JOM, Vol. 73, No. 12, 2021
https://doi.org/10.1007/s11837-021-04970-x

Corrosion, Wear and In-vitro Biocompatibility Property of Surface Mechanical Attrition Treatment Processed Ti-6Al-4V Alloy

SWARNIMA SINGH,[1] KRISHNA KANT PANDEY,[1] VAMSI KRISHNA BALLA,[2] MITUN DAS,[2] and ANUP KUMAR KESHRI [1,3]

1.—Metallurgical and Materials Engineering, Indian Institute of Technology Patna, Patna, Bihar 801106, India. 2.—Bioceramics and Coating Division, CSIR-Central Glass and Ceramic Research, Kolkata 700032, India. 3.—e-mail: anup@iitp.ac.in

The present study aims to understand the influence of surface mechanical attrition treatment (SMAT) on corrosion, wear, and in vitro cell viability of Ti-6Al-4V alloy. XRD analysis quantified the extent of surface nanocrystallization and the induced strain, which increased from 0.096 ± 0.021 to 0.166 ± 0.039, and so did dislocation density (from 1.55×10^{22} to 4.62×10^{22}). TEM analysis advocated for grain refinement and also manifested the occurrence of mechanical twins as well as dislocation walls in the SMATed surface. SMAT processing decreased the corrosion rate in simulated body fluid by ~75%, from 0.167 ± 0.097 mpy to 0.040 ± 0.015 mpy. This was attributed to the nanocrystallization that led to the creation of a stable and insoluble TiO_2 passive film at the interface of the surface and electrolyte. Grain refinement of the SMATed surface also derived an improvement in the wear resistance and cell adhesion property.

INTRODUCTION

In the past few decades, surface nanocrystallization of materials, owing to one of the most advanced processes in the turf of physical metallurgy, has attracted significant attention in the scientific community.[1–5] The usually employed methods for producing the nanostructured surfaces are classified under the family of severe plastic deformation (SPD). Of the SPD techniques, surface mechanical attrition treatment (SMAT) has stood out as an effective technique in the past few years. During SMAT, balls of 2 mm–10 mm diameter are randomly shot upon a substrate with a velocity interval of 5–15 m/s to generate a nanostructured surface. Many works have already been carried out to generate nanostructured surfaces on various metallic alloys, such as Ti-6Al-4V, low carbon steel (LCS), stainless steel, copper, etc. SMAT alters the properties of metallic surfaces, specifically corrosion, mechanical, and wear behavior, with continuous repetitive shots.[1–12] So far, controversial outcomes on the properties of the SMATed surfaces have been reported.

For example, a few researchers reported an upsurge in the corrosion resistance (CRes) of metallic surfaces;[7,13,14] others revealed the reversed trend for the same.[5,15,16] The improvement in CRes was accredited to the development of a stable passive layer over the produced nanostructured surface due to the presence of dense dislocation boundaries. These dislocation boundaries were a result of continuous shooting of the balls upon the sample surface during SMAT. On the other hand, the slowing of the same property was found mainly because of less treatment time or due to larger ball size that provided higher pit-to-peak ratios. The higher pit-to-peak ratio results in a higher diffusion of the corrosive electrolyte through the SMATed surface.[5,10,15] Similar contradicting results have been reported for the wear behavior, too. An increase in the surface hardness and roughness along with improved induced compressive residual

(Received June 24, 2021; accepted October 3, 2021; published online October 28, 2021)

stress led to an enhancement in the wear resistance,[1,17,18] whereas the reduction in ductility after the treatment displayed an adverse effect.[1]

Few works on the effect of SMAT on the wear and corrosion properties can also be found for Ti-6Al-4V alloys. Jelliti et al. created a nanostructured surface on Ti-6Al-4V alloy using SMAT for different periods and studied their corrosion behavior in Ringer's solution. They observed that a processing time of ~20 min provided a relatively better corrosion resistance of the surface compared to that of the surface treated with a processing time of ~15 min. While the shorter duration treatment provided only TiO_2 film as a shielding film onto the sample surface, a relatively higher duration treatment could impart a much stable passive film as a combination of Ti_2O_3 and TiO_2 films.

Contrary to the above results, a lower duration of SMAT seems logical for the enhancement in the wear property of the same alloy. Kumar and coworkers used 5-mm steel balls to perform SMAT over Ti-6Al-4V alloys for different periods of 30 min and 60 min. A higher ductility was noticed for the 30 min-treated sample, which favored its higher wear resistance. They observed that as the SMAT period increased, higher brittleness along with hardness was induced in the sample. This increase in brittleness occasioned the development of harder debris at the boundary of the alumina ball and the sample during the wear test, which accelerated the wear process further. Hence, it can be pointed out that relatively lower SMAT duration favors better wear resistance, which is in contrast with the corrosion result.

Additionally, if Ti-6Al-4V is employed as an implant, then the nature of its interaction with the in-body biological environment is of great importance. Several studies have reported different behaviors of the nanostructured titanium (Ti) toward the cell culture and osteoblast adhesion onto their surface.[19–24] Huang et al. refined the grain size of Ti alloy from 110 μm to 26 nm using SMAT. They found a significant enhancement in the osteoblast adhesion for the nano-grained Ti surface compared to the untreated sample.[19] Zhao et al. reported an improvement in the adhered cell quantity on the SMATed Ti surface compared to the bare surface.[23] The reasons were attributed to the grain refinement of the surface as well as an increase in the surface roughness of the sample after SMAT. Contrarily, Acharya et al. observed no improvement in the osteoblast growth and its adhesion on the Ti alloy after SMAT.[24] Hence, the effect of SMAT over the implant on the osteoblast attachment and growth still feels masked.

From the above discussion, it can be deduced that though few works have been carried out separately on the wear and corrosion properties for the SMATed Ti-6Al-4V surface, a clear understanding of the investigated properties is still missing. Also, the effect of surface nanocrystallization on the osteoblast performance of SMATed Ti-6Al-4V surface has never been manifested. Hence, the current work attempts to provide an overall effect of SMAT on the corrosion and wear behavior as well as on the osteoblast performance of Ti-6Al-4V alloy. We are aiming to create a nanostructured surface over the Ti-6Al-4V alloy using SMAT. Post-treatment, the phase analysis of the SMATed surface will be verified by x-ray diffraction (XRD). The grain size and microstructure of the SMATed surface will be evaluated using field emission scanning electron microscopy (FESEM), transmission electron microscopy (TEM), etc. The consequence of surface nanostructure on the corrosion, tribological properties and osteoblast performance of Ti-6Al-4V alloy will be investigated in detail.

EXPERIMENTAL METHODS

Preparation of SMATed Surface

SMAT process was executed using the surface nanocrystallization equipment from SNC (Chengdu SNC, Advanced Technology, Co, Ltd., China) for 90 min, and Fig. S1 depicts the schematic (mentioned in the supplementary file as Fig. S1). The Ti-6Al-4V substrate ($10 \times 2 \times 0.3$ cm^3) and spherical stainless-steel balls (∅: 4 mm) were placed inside a vacuum chamber (vacuum level = 0.1 MPa). The reason for choosing the 4-mm balls has been highlighted in our earlier study.[25] The vacuum chamber was vibrated with the help of a vibration generator. This produces a vibrating frequency of 50 Hz, forcing the balls to hit the sample surface from a random direction. Each impact on the sample surface tends to induce a higher strain rate and manipulate the respective microstructure of the substrate

Phase and Microstructural Observation After SMAT

Phase identification of the bare and SMATed surface was accomplished using x-ray diffractometer (Rigaku, TTRAX III, Japan). The 2θ range was maintained as 20–90° at a scan speed of 2°/min by Cu-K_α source with a wavelength of 1.54 Å. For a quantitative overview, XRD peaks were analyzed to find the values of change in the crystallite size and lattice strain. The dislocation density of the samples after SMAT was also tabulated using the XRD pattern. The crystallite size (D) and microstrain (ε) were calculated by using Scherrer Eqs. 1 and 2, respectively, i.e.,

$$D = \frac{0.9\lambda}{b \cdot \cos\theta} \tag{1}$$

$$\varepsilon = \frac{\beta}{4\tan\theta} \tag{2}$$

where λ denotes the respective x-ray wavelength and b is full width at half maxima (FWHM). θ

denotes the Bragg's angle, and β is peak broadening due to deformation.[14,25] Furthermore, the dislocation density (ρ) of the samples was calculated by using the crystallite size and microstrain as per equation

$$\rho = \frac{3\sqrt{2}\pi\varepsilon}{D\forall} \quad (3)$$

where $\forall$ denotes Burgers vector. $\forall$ is calculated as $\sqrt{a^2 + c^2}$, where a and c are the lattice constants for Ti (a = 0.295 nm and c = 0.468 nm).[14,27] FE-SEM (JSM –6010LA, JEOL, Japan) and optical profilometer (Zegage Ametex, Ultra-precision Technologies, Berwyn) provided a visual perspective of the modified surface of Ti-6Al-4V with respect to the bare surface. Transmission electron microscope (JEOL JEM 200 CX, Japan) was used extensively for the study of nano-crystallized surfaces.

Electrochemical Tests of the SMATed Surface

The corrosion behavior of the surfaces was measured by electrochemical tests executed in simulated body fluid or Ringers' solution. Ringer's solution contained a mixture of 9 g NaCl, 0.24 g $CaCl_2$, 0.2 g $NaHCO_3$ and 0.42 g KCl in 1 L distilled water.[28] Each test was repeated at least three times to certify the repeatability of the obtained results. The polarization tests and EIS were performed using a GAMRY electrochemical workstation (Interface 1000, Gamry, USA). Open circuit potential (OCP) measurement was performed for 2 h to attain stability. Bare and SMATed Ti samples were used as the working electrodes distinctly. The exposure area of the working electrodes was maintained as 1 cm^2. The potential window for the potentiodynamic test was maintained between − 0.25 V to 0.5 V at a rate of 1.6 mV/s. The Tafel extrapolation method provided the corrosion current density and the corrosion potential of the corresponding samples. The corrosion rate was obtained using Eq. 4,[26]

$$\mathrm{CR} = \frac{K_1 i_{\mathrm{corr}} \mathrm{EW}}{\rho} \quad (4)$$

where CR is the corrosion rate of the sample with a unit of mils per year (mpy), K_1 is constant with a value of 1.288 × 10^5 mils/(A.cm.year), and i_{corr} denotes the corrosion current density of the sample obtained by extrapolating the Tafel curve. EW and ρ denote the equivalent weight and density of the samples, respectively. The frequency range for EIS measurement was set from 100 kHz to 10 mHz with a 10 mV AC excitation potential.

Wear Behavior of the SMATed Surface

Room temperature dry wear performance of the surface was determined using a ball-on-disc tribometer (Ducom Instruments, Bangalore, India). A load applied on the sample was kept constant at 1 N with a track radius of 7.5 mm with a speed of 250 rpm. The total running length of the steel ball (counterpart) during the experiment was maintained as 500 m. Specific wear rate (R) of the samples was calculated using the formula,

$$R = \frac{V}{F \cdot s} \quad (5)$$

V is the wear volume, F is the normal load (N), and s is the sliding distance (m). Since F and s are constant during the experiment, the wear rate solely depends on the volume of material removed during the test. For obtaining an average value of the wear rate for each substrate, the wear experiment was repeated five times for each substrate.

In Vitro Cell Culture Experiment

In vitro cell culture experiments were completed on gamma-ray sterilized (25 kGy) ∅ 10 mm disk samples, using MG63 cells. Routine culturing of the cells was performed as per standard protocol, at 37 °C with 5% CO_2 and 95% humidity.[29,30] The confluent cells (10 × 10^3 cells/sample) were seeded onto the samples, and then 1 ml α-MEM was added. The well plates with cell-seeded samples (n = 3) were placed in an incubator at 37 °C with 5% CO_2. The culture duration was 2, 4 and 6 days with culture media change on every alternate day. After each culture duration, the cell viability on these samples was assessed using 3-[4,5-dimethylthiazol-2-yl]-2,5-diphenyltetrazolium bromide (MTT) assay (Sigma, St. Louis, MO, USA) following the procedure reported earlier.[29,30]

RESULTS AND DISCUSSIONS

Phase Evaluation and Microstructural Characterizations

Figure 1a shows the XRD pattern of the untreated as well as the SMATed Ti-6Al-4V alloy. The XRD pattern has mainly shown the presence of α-Ti phase in both the cases, with a minor diffraction peak of β-Ti (110), which is nearly overlapping with that of α-Ti (002) and α-Ti (101). The emergence of the new peak was observed in the SMATed sample, i.e., TiO_2 (202), as shown in Fig. 1B. Furthermore, peaks of the SMATed Ti-6Al-4V samples were found to be relatively broader with respect to those of untreated samples. Table I confirms the average FWHM value of the peaks showing a two-fold increase for the SMATed surface. This peak broadening usually happens when the coarser grains are transformed into finer ones, more specifically into nano-sized grains. The calculated crystal size for both the samples have been provided in Table I, showing a decrease in crystallite size from 104 ± 14 nm (untreated) to 60 ± 9 nm (treated). The decrease in the grain size suggests the disintegration of coarser grains into finer ones because of the impingement of high-velocity balls at the surface.

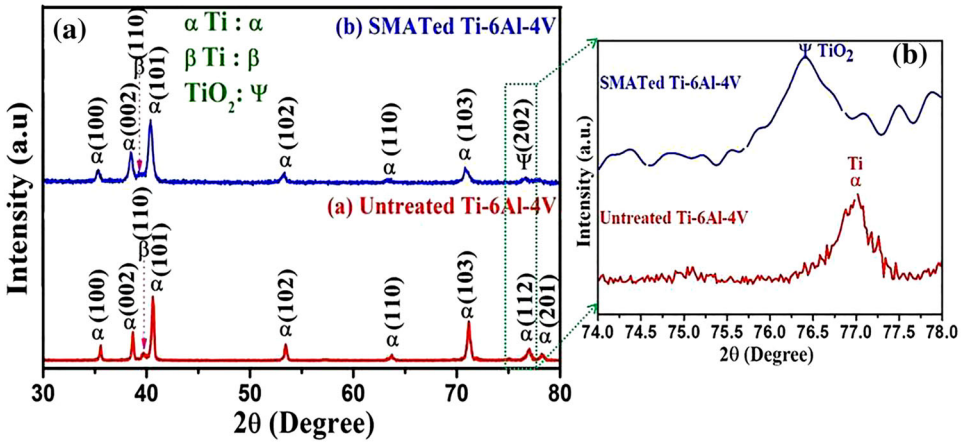

Fig. 1. XRD pattern of (a) untreated and SMATed Ti-6Al-4V surface (b) magnified XRD pattern between 74–78°

Table I. Crystallite size, microstrain and dislocation density of untreated and SMATed Ti-6Al-4V

S. No.	Nomenclature	FWHM	Crystallite size (D) nm	Microstrain (ε)	Dislocation density (m^{-2})
1	Untreated	0.269 ± 0.057	104 ± 14	0.096 ± 0.021	1.550×10^{22}
2.	SMATed	0.629 ± 0.168	60 ± 9	0.166 ± 0.039	4.620×10^{22}

Besides this, a shift in the peaks toward the left has also been observed for the SMATed surface, which is a sign of induced strain. Table I provides the microstrain value of 0.096 ± 0.021 for the bare surface, which increased to 0.166 ± 0.039 after the SMAT processing. This strain is mainly a result of repetitive shots of the steel balls onto the sample, which resulted in compression of the substrate surface.[31,32] Interestingly, a lessening in the peak height is also remarked for the SMATed surface, attributed to both effects, i.e., drop in the grain size as well as an increase in microstrain. One more aspect of SMAT can be specified as the alteration in the dislocation density of the surface. As the microstrain in the surface increases with subsequent impact, the population density of dislocations also increases. Table I exhibits an increase in dislocation density of SMATed surface by nearly three fold compared to the bare surface, from 1.550 $\times 10^{22}$ m^{-2} to 4.620 $\times 10^{22} m^{-2}$.

Figures S2a and b portray the FE-SEM image of both surfaces while Fig. S2c and d is the optical profilometer image (shown in the supplementary file as Fig. S2). As seen in Fig. S2a, the FE-SEM image depicts the smooth surface and is free from any visible dents or cracks. However, the SMATed surface shows the rough surface indicating the metal flow and non-uniform pile-up. Figure S2c shows the almost flat profile of the untreated surface without any cracks, deformations or pores in it. The same surface gets severely plastically deformed after the SMAT takes place, as visualized in Fig. S2d. The continuous bombardment of shots on the surface leads to the formation of several surface pits, initiating metal flow near these pits forming newer peaks and valleys compared to the untreated one.[33] The average surface roughness increases by more than two times from 0.08 μm for untreated to 0.18 μm in SMATed surface.

TEM Evaluation of the SMATed Surface

Darkfield TEM images of the untreated and SMATed surface are shown in the Fig. 2a and b, which reveals the extent of the nanocrystallization generated over the SMATed surface. Also, Fig. 2a and b display the grain morphology before and after the surface treatment, respectively, whereas 2c and 2d show the histogram for the corresponding grain size variation. The untreated surface has coarser grains with a maximum grain size of 160 nm and mean grain size of 63 ± 10 nm (Fig. 2c), while the SMATed surface shows a mean grain size of 18 ± 3 nm, with no grains exceeding the maximum size of 35 nm (Fig. 2d). This difference in grain sizes indicates the grain refinement process takes place over the Ti-6Al-4V surface. A difference in the mean grain size measured using TEM and XRD is quite evincible, with the former having the lesser value. However, both investigations indicate an overall similar trend where the coarser grains of untreated surface converted into much smaller ones after SMAT processing.

Moreover, the grain refinement taking place due to SMAT is a multi-route process that dominantly arises from the formation of mechanical twins on the adjacent surface microstructure. Figure 3a shows a TEM image of the presence of mechanical

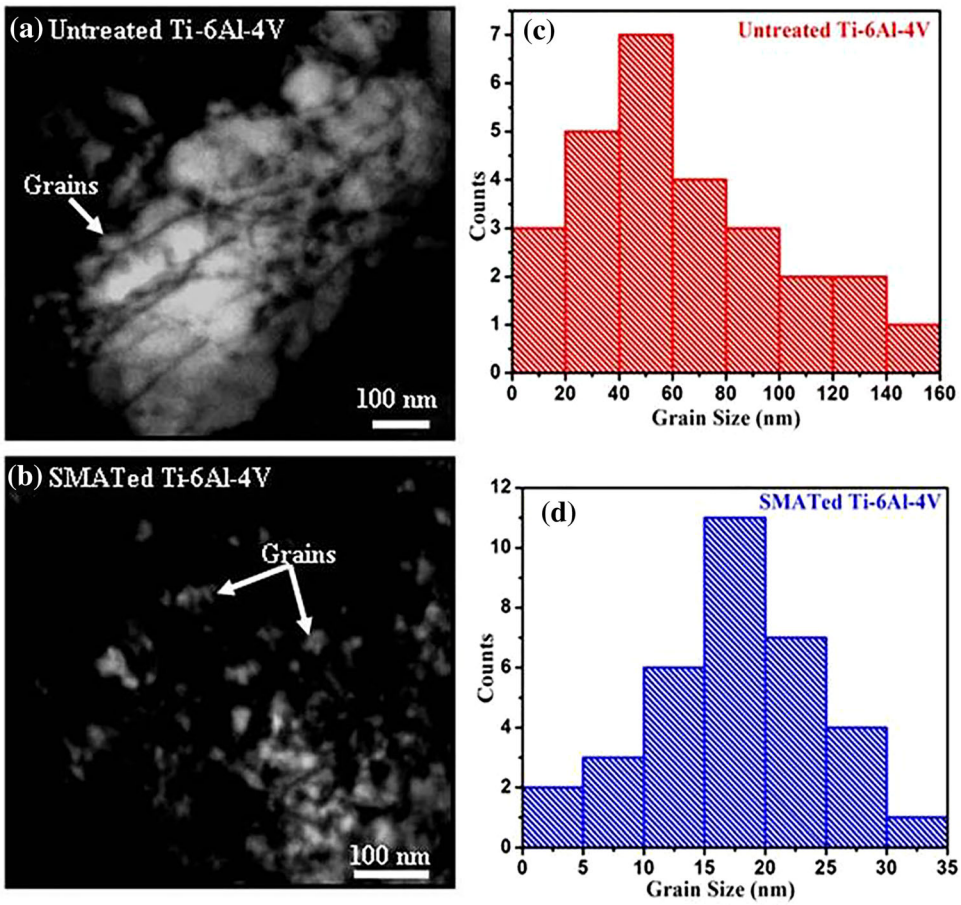

Fig. 2. TEM dark-field images of (a) untreated Ti-6Al-4V surface; (b) SMATed Ti-6Al-4V surface; (c-d) respective grain size distribution.

twins on the SMATed surface. Furthermore, as the strain rate increases because of repetitive shots, these twins increase in number and start to intersect the path of neighboring twins. This twin crossover limits the relative atomic movement within the microstructure, restricting further gross deformation due to the mechanical twins. Chichili et al. also report that mechanical twins contribute to not more than 15% of the total strain during the cold-working of Ti.[34] Furthermore, as the impingement of balls on the surface proceeds, many twins intersect with each other and hinder the propagation of the dislocations resulting in the increased dislocation density within the microstructure. This secondary phase, i.e., multiplication of the dislocations, leads to grain subdivision of the microstructure till it reaches a nanometric range. Figure 3b shows a high magnification TEM image of the nano-crystallized surface, and Fig. 3c is the inverse fast Fourier transform image (IFFT) of a selected region of Fig. 3b displaying the numbers of edge dislocations. On increasing strain over the surface, a few dislocation walls cut among themselves and give birth to two similar dislocation walls (i.e., negative dislocation) providing tensile stress on the microstructure. Contrarily, few dislocations coalesce to merge into one (i.e., positive dislocation) giving compressive stress in return. These positive and negative dislocations arise over the whole surface, turning the surface into a series of dislocation grids. These dislocation grids are a sign of the stretching out of atomic bonds on the surface plane giving rise to nano-level lamellae. The continuous formation of lamellae further responds as a refined and nanostructured surface. Consequently, it can be seen that the total surface modification in the current work mainly consists of two modes of deformation, mechanical twinning followed by high dislocation density. Zhu et al. also provided a similar finding for the surface modification in α-Ti.[35] Initially, at lower strain, twinning plays a prominent role in deformation, but it amounts to a much lower percentage of the plastic strain. With the increase in strain, the deformation by dislocation surpasses the twinning mode of deformation, and the formation of nanograins is observed as a complementary action of these two deformation modes. This grain refinement is expected to increase the corrosion, tribological as well as osteoblast adhesion properties of the surface, which is discussed in the upcoming sections.

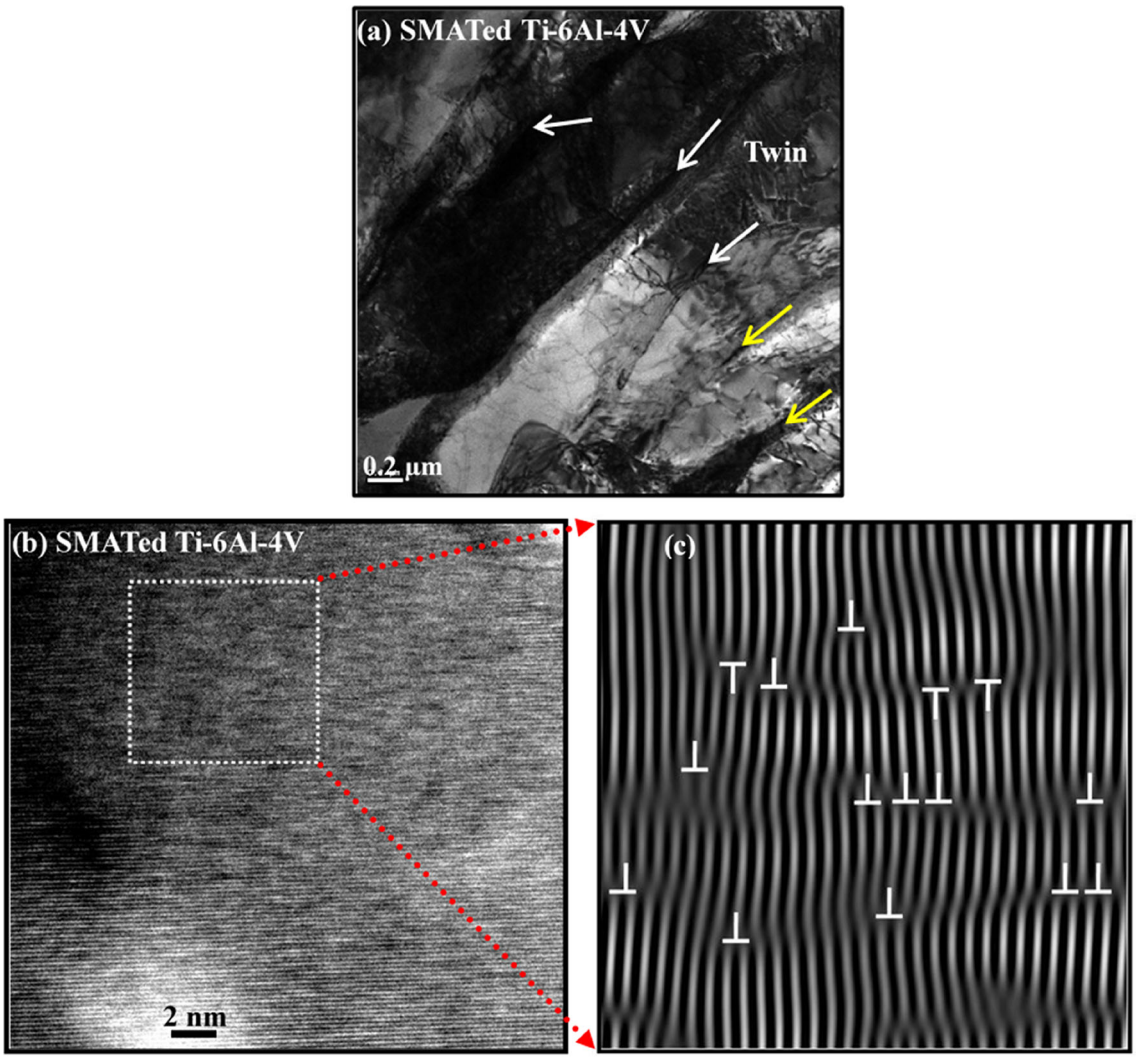

Fig. 3. (a) TEM images shows the twin planes (arrows). (b) High-magnification TEM image of SMATed Ti-6Al-4V surface (c) showing the edge dislocation obtained using the inverse fast Fourier transform (IFFT) from the marked square in (b).

Electrochemical Response of the Original and SMATed Ti-6Al-4V Samples

Figure 4a demonstrates the timely progress of open circuit potential (OCP) for SMATed surface with reference to the untreated one. The OCP of the untreated surface was measured as − 0.45V, whereas it stabilized at − 0.22 V for the SMATed surface. The shift of the OCP toward a positive value suggests that there might be a development of a stable passive layer at the junction of the electrolyte and the SMATed surface. A large difference between the starting and final potential values for the untreated surface can be directed to the presence of coarser grains. In general, a coarser grain size routes to the emergence of the less stable passive layer at the electrolyte-sample interface compared to the nanosized grains.

Figure 4b shows the potentiodynamic polarization plot of untreated and SMATed surfaces. From this figure, E_{corr} and i_{corr} are tabulated in Table II. The untreated surface showed i_{corr} value of 0.489 μA/cm^2 that reduced by ~75% to a value of 0.119 μA/cm^2 for the SMATed surface. CR showed a drop of ~4 times for the SMATed surface with respect to the untreated surface. The breakdown potential (E_p) implies where the passive layer starts to degrade, while passive current density (i_p) indicates the passivation region. After the SMAT process, a decrease in i_p and increase in E_b were seen compared to the untreated sample, indicating the increase in corrosion resistance after SMAT. The reason for the improvement of the CRes of the SMATed sample lies in grain refinement. The refinement from coarser grains to nanograins increases the grain boundary area. As a result, electron activity increases at the grain boundaries, subsequently decreasing the electron work function. Electron work function (EWF) is the smallest amount of energy required to pull out an inner-core electron of the material.[36,37] Li and Li used an electrostatic action model to show the dependency of

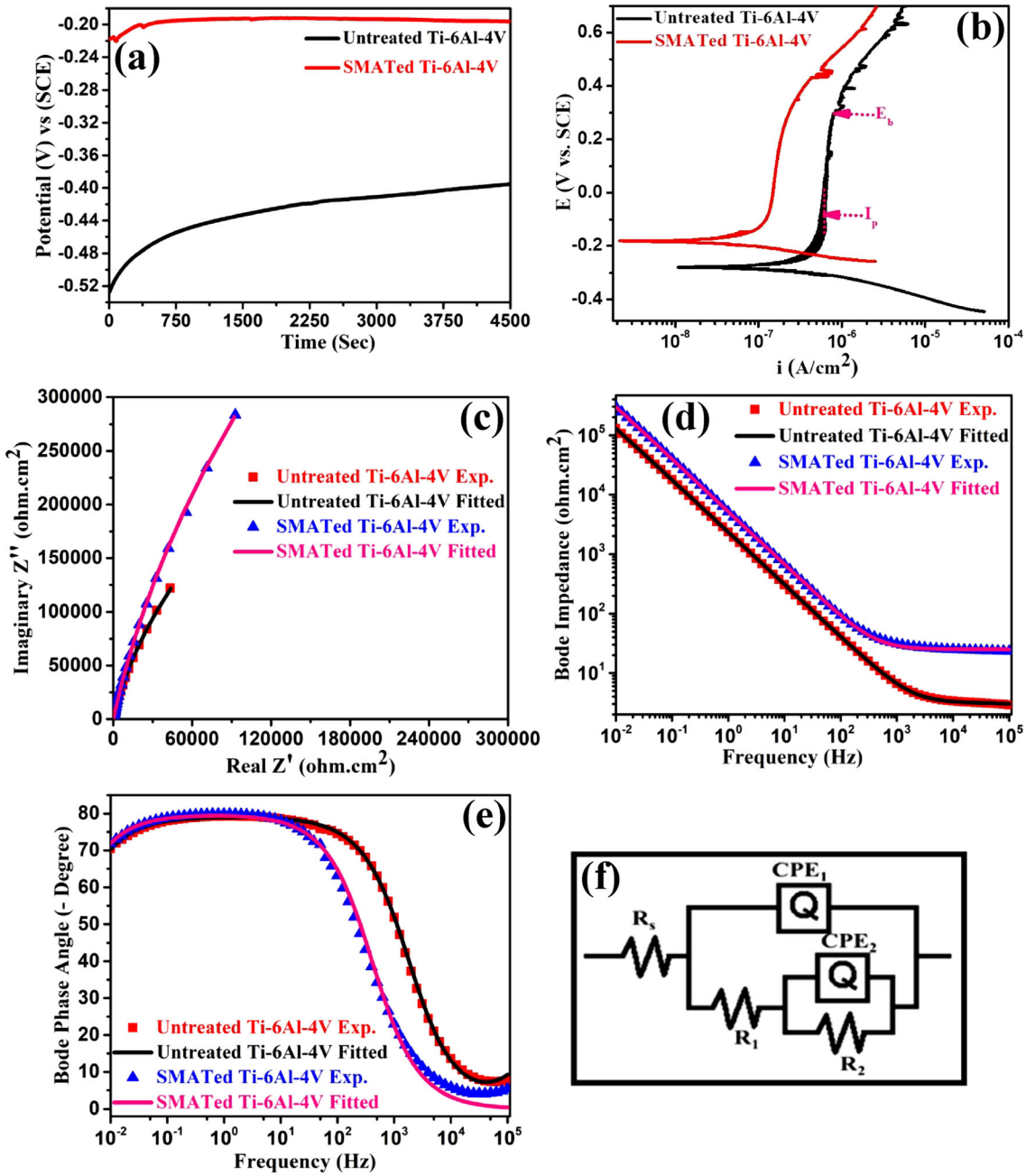

Fig. 4. (a) OCP curve. (b) Polarization plots and (c-e) EIS curve, i.e., Nyquist plot, Bode impedance and phase angle. (f) Equivalent circuit used for fitting EIS data of untreated Ti-6Al-4V and SMATed Ti-6Al-4V in Ringer's solution.

Table II. The polarization parameters of the Ti-6Al-4V samples before and after SMAT

S. No.	Nomenclature	i_{corr} (μA/cm^2)	E_{corr} (V versus SCE)	CR (mpy)
1.	Untreated	0.489 ± 0.112	− 0.279 ± 0.106	0.167 ± 0.097
2.	SMATed	0.119 ± 0.045	− 0.182 ± 0.073	0.040 ± 0.015

EWF on the dislocation of a system.[37] A decrease in the value of EWF increases the electron activity at the dislocation walls, which plays in favor of the CRes property of the SMATed surface. A more electrochemically active surface improves the passivation potential capability of SMATed surface; hence, the nano-sized grains can create a stable passive layer at the interface, namely TiO_2. The TiO_2 passive film remains insoluble in the simulated body fluid and provides better CRes to the body. A similar work was carried out by Thomas and coworkers, where they used the secondary ion mass spectrometry (SIMS) technique to estimate the oxygen percentage on the surface of α-Ti before and after nanocrystallization.[38,39] They revealed that the twin boundaries, as well as the dislocation bands with the deformed layer, improved the diffusion sites for oxygen, which ultimately increases the oxygen content over the Ti surface after nanocrystallization. The effect of surface modification on the CRes of the Ti-6Al-4V alloys was shown by Jelliti et al., where they found traces of oxygen (O) on the Ti surface after the surface modification.[6] They considered the occurrence of O from TiO_2, which validates the occurrence of TiO_2 (using XRD) in the current study. Acharya and the group have also reported an increase in the CRes of the Ti alloy after SMAT due to improvement in its passivity.[24]

Figure 4c, d, and e illustrates the Nyquist, Bode impedance and phase angle plot, respectively, for untreated and SMATed surfaces. Figure 4c shows that the SMATed surface has a higher loop, proving an improved CRes compared to the untreated surface. Similarly, a higher impedance for the entire range of frequency for the SMATed surface further attests to its better corrosion due to surface modification (Fig. 4d). Figure 4f represents the equivalent circuit model to fit the EIS results for analyzing the electrochemical reaction mechanism of the samples. The Reap2cpe model is used to fit the EIS plots of both samples. The high chi-square value validates the best fitting. The nomenclature of various parameters of the fitted model can be symbolized as

R_s = solution resistance

R_1 = pore resistance on the outer oxide layer of sample

R_2= resistance from inner passive film

CPE_1= constant phase element (CPE) of the outer oxide layer

CPE_2 = CPE of the interfacial electrical double layer (EDL) between oxide layer and substrate.

n = factor for determining the nature of CPE

The values of the different parameters of the equivalent circuit model are quantified in Table III. The values of R_1 and R_2 have a higher value for the SMATed surface in contrast to the untreated surface. This signifies the formation of a stable as well an insoluble passive oxide film after the SMAT processing. This film efficiently blocks the penetration of the Cl^- ion at the interface of the SBF, and the SMATed surface thus increases the CRes of the same. Shukla and the group also found higher CRes of nano-grained Ti compared to commercial pure Ti. They attributed this improvement to better interface adherence of passive film because of the highly dense grain boundaries of the ultrafine-grained Ti.[40] This signifies that SMATed Ti-6Al-4V alloy performs well in the corrosive environment of SBF and makes it suitable for implant purposes.

To show the extent of corrosion on the treated surface, topographical images obtained from the optical profiler are provided in the supplementary file as Fig. S3. The severity of corrosion on the untreated as well as SMATed surface is shown in Fig. S3a and S3b. Untreated surface manifests an alarming behavior in the corrosive environment of SBF, attributed to the larger pits on its surface where the ion transfers between the solution and the exposed area of the sample become easy. The black region in the topographical images denotes the pits on the surface, whereas the red portion symbolizes the corroded region accompanying the pits present. The yellow zone of the microstructure characterizes the corrosion-free surface. The higher the yellow region on the surface is, the more corrosion resistant the material in the SBF. Comparing both the treated and untreated surfaces indicates that SMAT processing not only provided the grain refinement, but also incorporated the heterogeneity over the surface. This heterogeneity made a path for the formation of stable passive film that resulted in sites less prone to electron exchange, as discussed earlier.

Wear Performance

Figure 5a shows the wear test result of the untreated and SMATed surface. With an applied load of 1N and a track radius of 7.5 mm, Fig. 5a

Table III. EIS fitted values of untreated and SMATed Ti-6Al-4V surface in Ringer's solution

S. No.	Sample	R_s ($\Omega \cdot cm^2$)	R_1 ($\Omega \cdot cm^2$)	R_2 ($k\Omega \cdot cm^2$)	CPE_1 ($S\ s^n\ cm^{-2}$) $\times 10^{-6}$	m	CPE_2 ($S\ s^n\ cm^{-2}$) $\times 10^{-6}$	n	Chi-square
1.	Untreated Ti-6Al-4V	3.06	546	133	46.20	0.86	84.21	0.90	1.73×10^{-4}
2.	SMATed 4 mm	23.12	835	317	14.90	0.81	37.92	0.88	1.69×10^{-4}

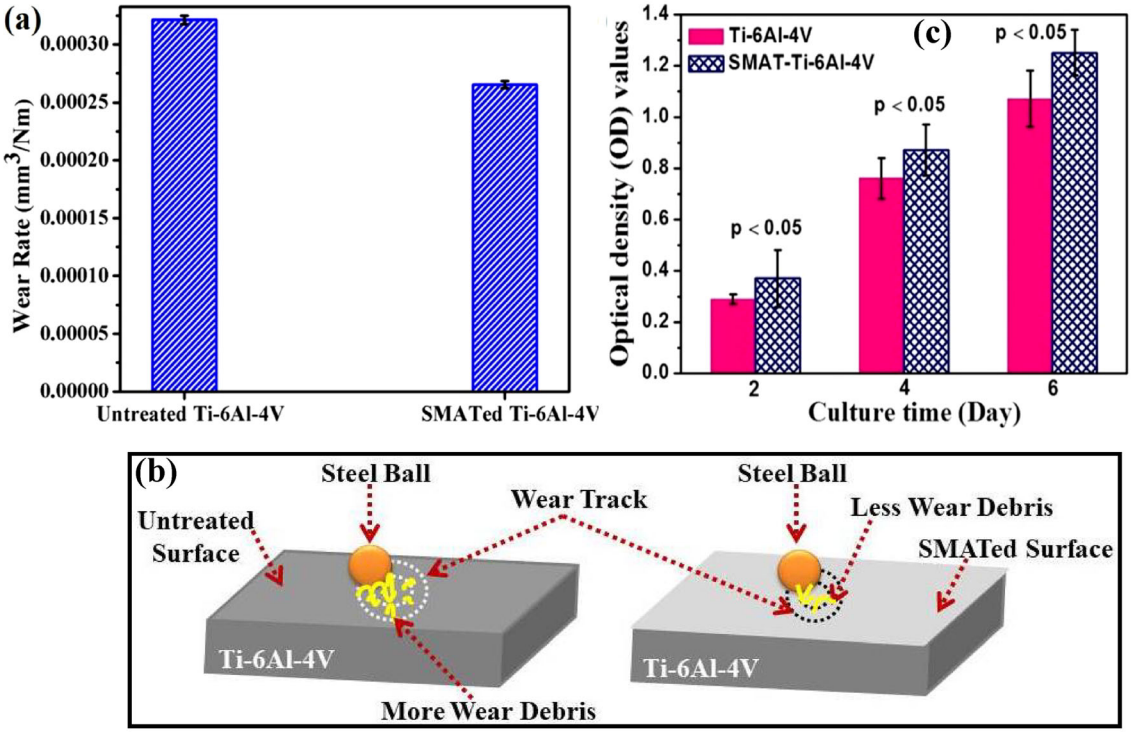

Fig. 5. (a) Wear rate, (b) schematic of the wear process and (c) cell culture results for the untreated and SMATed samples.

compares the wear behavior of the untreated and SMATed surfaces. The wear rate of the untreated surface was found to be $3.23 \times 10^{-4} \pm 0.27 \times 10^{-4}$ mm^3/Nm, which decreased to $2.51 \times 10^{-4} \pm 0.20 \times 10^{-4}$ mm^3/Nm for the SMATed surface. The increased wear rate and surface roughness of the untreated surface are attributed to the three-body abrasion wear mechanism (shown as schematic in Fig. 5b) induced by the abrasive hard wear debris generated from tribochemical reaction between Ti-6Al-4V sample and steel ball. Post-wear optical profiling image (Fig. S4) shows relatively higher roughness of the untreated surface, which could be due to large generation of wear debris. The reasons for the improved wear properties may be credited to the development of nanograins over the unabridged sample surface after SMAT. The grain boundaries restrict the further propagation of the cracks through them and prevent the nanograins from turning into loose debris during the wear process. Also, the formation of a thin ceramic film, i.e., TiO_2, over the SMATed surface could have provided a higher resistance against the pin during the wear process and improved its wear resistance. Xia et al. also provided an increase in the wear resistance of SMA treated magnesium alloy and concluded that the distribution of the oxide layer on the sample surface acted as a protection against wear.[4]

In Vitro Biocompatibility

Figure 5c compiles the MTT assay result of the MG63 cells cultured for different durations. The optical density values of the osteoblasts cultured on the untreated and the SMATed surface for 2, 4 and 6 days. During all the culture experiments, the growth rate was maintained to a value < 0.05 ($p < 0.05$). It can be seen since the start (day 2) that the absorbance level or the optical density of the osteoblasts on the SMATed surface was more than that on the untreated one. Even tough the values were increasing for both surfaces with an increase in the number of culture durations, the untreated surface remained lower than the SMATed surface. The increase in the absorbance for the SMATed surface could be ascribed to the upsurge in the proliferation of the cells.[23]

The grain refinement as well as an increase in roughness of the SMATed surface provided a larger number of active sites for the cell attachment. These improved characteristics, in turn, enhanced the surface energy of the SMATed surface, which is necessary for improving the cell response.[23,24] The higher surface energy of the SMATed surface stimulates the bonding of the cells with the surface, making it a better cellular adherent.[41]

CONCLUSION

SMAT resulted in surface nanocrystallization by reducing the grain size of the surface from 104 ± 14 nm on the untreated surface to 60 ± 9 nm on the SMATed surface. The strain induced in the sample increased from 0.096 ± 0.021 to 0.166 ± 0.039 after SMAT, while dislocation density enhanced from 1.550×10^{22} to 4.620×10^{22} (SMATed). TEM

exhibited the emergence of mechanical twins and dislocation walls in the SMATed Ti-6Al-4V sample in addition to the reduced grain size. Electrochemical tests assured a decrease in CR by ~75% after SMAT. Corrosion current density reduced from 0.489 $\mu A/cm^2$ to 0.119 $\mu A/cm^2$ for the nanostructured sample. Grain refinement assisted the formation of stable and insoluble passive TiO_2 film over the SMATed surface. Wear resistance of the SMATed surface improved with a ~23% decrease in wear rate, which may be credited to the formation of nanograins over the whole surface or to the creation of stable TiO_2 film over the surface. Cell culture results also showed improvement after SMAT, accredited mainly to the grain refinement, increase in surface roughness as well as the higher surface energy of the sample post-SMAT.

ACKNOWLEDGEMENTS

Dr. Swarnima Singh and Dr. Anup Kumar Keshri acknowledge IIT Patna for providing its research facilities. The authors also thank Dr. Lokesh Chandra Pathak and Dr. Siva Kumar Bose from CSIR- NML, Jamshedpur, for providing the SMAT equipment.

CONFLICT OF INTEREST

On behalf of all authors, the corresponding author states that there is no conflict of interest.

SUPPLEMENTARY INFORMATION

The online version contains supplementary material available at https://doi.org/10.1007/s11837-021-04970-x.

REFERENCES

1. S. Anand Kumar, S. Ganesh Sundara Raman, T.S.N. Sankara Narayanan, and R. Gnanamoorthy, *Adv. Mater. Res.* 463–464, 316–320. (2012).
2. K. Lu, and J. Lu, *Mater. Sci. Eng. A* 375–377, 38–45. (2004).
3. H. Wei, Y. Cui, H. Cui, C. Zhou, L. Hou, and Y. Wei, *J. Alloys Compd.* 763, 835–843. (2018).
4. S. Xia, Y. Liu, D. Fu, B. Jin, and J. Lu, *J. Mater. Sci. Technol.* 32, 1245–1252. (2016).
5. B. Thangaraj, S.N.T.S. Nellaiappan, R. Kulandaivelu, M.H. Lee, and T. Nishimura, *ACS Appl. Mater. Interfaces* 7, 17731–17747. (2015).
6. S. Jelliti, C. Richard, D. Retraint, T. Roland, M. Chemkhi, and C. Demangel, *Surf. Coatings Technol.* 224, 82–87. (2013).
7. T. Fu, Z. Zhan, L. Zhang, Y. Yang, Z. Liu, J. Liu, L. Li, and X. Yu Surf, *Coatings Technol.* 280, 129–135. (2015).
8. M. Wen, J.F. Gu, G. Liu, Z.B. Wang, and J. Lu, *Surf. Coatings Technol.* 201, 6285–6289. (2007).
9. T. Balusamy, T.S.N. Sankara Narayanan, K. Ravichandran, I.S. Park, and M.H. Lee, *Corros. Sci.* 74, 332–344. (2013).
10. T. Balusamy, S. Kumar, and T.S.N. Sankara Narayanan, *Corros. Sci.* 52, 3826–3834. (2010).
11. Z.B. Wang, N.R. Tao, S. Li, W. Wang, G. Liu, J. Lu, and K. Lu, *Mater. Sci. Eng. A* 352, 144–149. (2003).
12. Y.S. Zhang, Z. Han, and K. Lu, *Wear* 265, 396–401. (2008).
13. L. Jin, W.F. Cui, X. Song, G. Liu, and L. Zhou, *Oral Oncol.* 50, 2529–2535. (2014).
14. S. Singh, K.K. Pandey, S.K. Bose, and A.K. Keshri, *Surf. Coat. Technol.* 396, 125964. (2020).
15. A.E. Hannora, *Mater. Res. Express* 6, 1–11. (2019).
16. W.Y. Guo, J. Sun, and J.S. Wu, *Mater. Charact.* 60, 173–177. (2009).
17. A. Amanov, I.S. Cho, D.E. Kim, and Y.S. Pyun, *Surf. Coatings Technol.* 207, 135–142. (2012).
18. S. Alikhani Chamgordani, R. Miresmaeili, and M. Aliofkhazraei, *Tribol. Int.* 119, 744–752. (2018).
19. R. Huang, L. Zhang, L. Huang, and J. Zhu, *Mater. Sci. Eng. C* 97, 688–697. (2019).
20. L. Weiss, Y. Nessler, M. Novelli, P. Laheurte, and T. Grosdidier, *Metals (Basel)* 9, 1–15. (2019).
21. B.C. Ward, and T.J. Webster, *Mater. Sci. Eng. C* 27, 575–578. (2007).
22. X. Liu, P.K. Chu, and C. Ding, *Mater. Sci. Eng. R Reports* 70, 275–302. (2010).
23. C. Zhao, P. Han, W. Ji, and X. Zhang, *J. Biomater. Appl.* 27, 113–118. (2012).
24. S. Acharya, A.G. Panicker, V. Gopal, S.S. Dabas, G. Manivasagam, S. Suwas, and K. Chatterjee, *Mater. Sci. Eng. C* 110, 110729. (2020).
25. T. Balusamy, T.S.N. Sankara Narayanan, K. Ravichandran, M.H. Lee, and T. Nishimura, *J. Electrochem. Soc.* 162, C285–C293. (2015).
26. S. Singh, M. Sribalaji, N.P. Wasekar, S. Joshi, G. Sundararajan, R. Singh, and A.K. Keshri, *Appl. Surf. Sci.* 364, 264–272. (2016).
27. A. Sohrabi, A. Dolati, M. Ghorbani, M.R. Barati, and P. Stroeve, *J. Phys. Chem. C* 116, 4105–4118. (2012).
28. S. Singh, K.K. Pandey, A. Islam, and A.K. Keshri, *Ceram. Int.* 46, 13539–13548. (2020).
29. C. Khatua, S. Sengupta, B. Kundu, D. Bhattacharya, and V.K. Balla, *Mater. Des.* 167, 107628. (2019).
30. N.C. Reger, B. Kundu, V.K. Balla, and A.K. Bhargava, *Int. J. Appl. Ceram. Technol.* 16, 503–516. (2019).
31. H. Kou, J. Lu, and Y. Li, *Adv. Mater.* 26, 5518–5524. (2014).
32. P. Tadge, and C. Sasikumar, *Trans. Indian Inst. Met.* 71, 1543–1552. (2018).
33. B. Arifvianto, and M. Mahardika, *Appl. Surf. Sci.* 258, 4538–4543. (2012).
34. D.R. Chichili, K.T. Ramesh, and K.J. Hemker, *Acta Mater.* 46, 1025–1043. (1998).
35. K.Y. Zhu, A. Vassel, F. Brisset, K. Lu, and J. Lu, *Acta Mater.* 52, 4101–4110. (2004).
36. D.Y. Li, *Mater. Res. Soc. Symp. Proc.* 887, 227–235. (2006).
37. W. Li, and D.Y. Li, *Mater. Sci. Technol.* 18, 1057–1060. (2002).
38. M. Thomas, T. Lindley, D. Rugg, and M. Jackson, *Acta Mater.* 60, 5040–5048. (2012).
39. M. Thomas, T. Lindley, and M. Jackson, *Scr. Mater.* 60, 108–111. (2009).
40. A.K. Shukla, R. Balasubramaniam, and S. Bhargava, *Intermetallics* 13, 631–637. (2005).
41. V.K. Balla, S. Dey, A.A. Muthuchamy, G.D. Janaki Ram, M. Das, and A. Bandyopadhyay, *J. Biomed. Mater. Res. Part B Appl. Biomater.* 106, 569–577. (2018).